
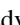
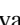




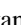
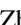


## Structure and electronic properties of amorphous strontium titanate

Julia E. Medvedeva <sup>1,\*</sup>, Bishal Bhattarai <sup>1</sup>, Ivan A. Zhuravlev <sup>1</sup>, Federico Motti <sup>2,3,4</sup>, Piero Torelli <sup>4</sup>, Anita Guarino <sup>4</sup>,  
Andreas Klein <sup>5</sup>, Emiliano Di Gennaro <sup>6</sup> and Fabio Miletto Granozio <sup>7</sup>

<sup>1</sup>Department of Physics, Missouri University of Science and Technology, Rolla, Missouri 65409, USA

<sup>2</sup>Laboratory for Mesoscopic Systems, Department of Materials, ETH Zurich, 8093 Zurich, Switzerland

<sup>3</sup>Laboratory for Multiscale Materials Experiments, Paul Scherrer Institute, 5232 Villigen PSI, Switzerland

<sup>4</sup>Institute of Materials, CNR, Trieste 34149, Italy

<sup>5</sup>Department of Materials, Technical University of Darmstadt, Darmstadt 64287, Germany

<sup>6</sup>Department of Physics, University of Naples Federico II, Naples 80126, Italy

<sup>7</sup>CNR-SPIN, University of Naples Federico II, Naples 80126, Italy



(Received 6 January 2022; revised 21 April 2022; accepted 7 July 2022; published 27 July 2022)

Understanding the short-range structure of an amorphous material is the first step in predicting its macroscopic properties. Amorphous strontium titanate (a-STO) presents a unique challenge due to contradictory experimental findings regarding the local oxygen environment of titanium, concluded to be either tetrahedral or octahedral. To elucidate the discrepancy, 72 models of a-STO with density ranging from the crystalline value 5.12 to 3.07 g/cm<sup>3</sup> were prepared using *ab initio* molecular dynamics liquid-quench simulations and characterized by extended x-ray absorption fine structure (EXAFS) for both Ti and Sr K edge. An excellent agreement between the calculated and two independent experimental EXAFS measurements demonstrates that the discrepancy in the Ti coordination stems from differences in the material's density. Next, density-dependent structural characteristics, including Ti-O and Sr-O coordination, distances, angles, polyhedral sharing, and vibrational density of states in a-STO are thoroughly analyzed and correlated with disorder-induced changes in the electronic properties that are calculated using a hybrid density functional. The obtained increase in the band gap and broadening of Ti-*d* *e<sub>g</sub>*-orbital contributions in the conduction band are in excellent agreement with our x-ray absorption spectroscopy for Ti L-edge spectra and optical absorption measurements for crystalline and amorphous STO grown by pulsed laser deposition. The derived microscopic understanding of the structure-property relationship in amorphous “perovskite” serves as a foundation for further investigations of a-STO and related materials.

DOI: [10.1103/PhysRevMaterials.6.075605](https://doi.org/10.1103/PhysRevMaterials.6.075605)

### I. INTRODUCTION

Technological appeal and several functional properties have driven the extensive research of strontium titanate, an important  $ABO_3$  perovskite. Crystalline  $SrTiO_3$  (c-STO) exhibits fascinating properties including ferroelectricity, piezoelectricity, ferromagnetism, superconductivity [1–7]. Accordingly, thin film dielectrics of crystalline  $ABO_3$  have various practical applications in electronic devices and memory cell capacitors [8,9]. c-STO is frequently used as a substrate material for fabrication of high-temperature superconducting materials, multiferroics, and manganites with singly terminated  $TiO_2$  layer crucial to grow complex oxide heterostructures [10]. However, thin-films c-STO suffer several limitations such as poor electrical properties as compared to bulk crystalline materials and high sensitivity on deposition process or heat treatment techniques [8].

Amorphous materials of  $ABO_3$  composition may provide an alternative route to attain structural stability with smooth surfaces while avoiding grain boundaries and internal lattice strain, and are readily synthesized by low-cost deposition

techniques [8,11,12]. Amorphous  $SrTiO_3$  (a-STO) thin films have been used to show excellent resistive switching performance for novel nonvolatile memory devices [13,14] and have been utilized as gate dielectric [15,16] in field-effect transistor. Additionally, amorphous and quasiamorphous phases of STO [17–20] have shown to exhibit polarity, opening a wide range of possible applications in electronic devices that prohibit utilization of c-STO due to fundamental or technological barriers [17,18].

Understanding how the local structure and morphology of perovskite materials change upon amorphization is key to establishing the structure-property relationships in the disordered materials and may open up new research avenues and opportunities [12,21–24]. For amorphous STO, the coordination of Ti remains under debate: while it is typically argued in literature that the good properties of a-STO are due to the  $TiO_6$  (octahedral) coordination being maintained in the disordered phase, two experimental studies that employed extended x-ray absorption fine structure (EXAFS) measurements infer contradictory results with octahedral [17] and tetrahedral [20] Ti coordination. Importantly, in contrast to amorphous  $TiO_2$  with covalent metal-oxygen bonds [25–35] or to ionic amorphous oxide semiconductors [36,37], a-STO is a mixed-metal oxide with covalent (Ti-O) and ionic (Sr-O) bonds. The presence

\*juliaem@mst.edu

of weaker (ionic) bonding implies that structural disorder is likely to manifest itself not only in a disrupted polyhedral network on the medium- and long-range scales—as evident from the suppressed EXAFS peaks beyond the first shell in a-STO as compared to c-STO [17]—but also in distortions within the individual metal-oxygen polyhedra, i.e., within the nearest-neighbor structure that determines the metal coordination and ultimately governs the electronic properties of the material.

In this work, first-principles density-functional approach is employed to accurately describe how the structural and electronic properties of STO change upon amorphization. To aid this computationally intensive study, we prepare 72 amorphous models of substoichiometric  $\text{Sr}_{26}\text{Ti}_{26}\text{O}_{77}$  with 129 atoms per cubic supercell and with density ranging within  $0.6\text{--}1.0\rho_c$ , where  $\rho_c = 5.12 \text{ g/cm}^3$  is the crystalline density of perovskite  $\text{SrTiO}_3$ . The choice of the supercell size of about  $11\text{--}13 \text{ \AA}$  for a-STO models is sufficient to accurately capture the structure in up to 5–6 shells in the disordered material, whereas the experimental EXAFS measurements [17] showed that the peaks beyond the first shell (Ti-O and Sr-O) are suppressed as compared to the crystalline STO phase. The amorphous structures are obtained using *ab initio* molecular dynamics (MD) melt-quench approach [39], whereas the electronic properties of the relaxed structures are calculated using hybrid density functional, as implemented in Vienna *ab initio* simulation package (VASP) [40,41], see Appendix for details. The density-dependent changes in the local structure of a-STO are analyzed using pair correlation function, angle distribution, effective coordination and distances, polyhedral linkages in the metal-oxygen network and compared to those in c-STO. Moreover, we calculate EXAFS spectra for both Ti and Sr K edge to directly compare our theoretical results with the available EXAFS measurements to validate the models. Next, the electronic, optical, and vibrational properties of c- and a-STO are determined. The results are in excellent agreement with our x-ray absorption spectroscopy (XAS) for Ti L-edge spectra and optical absorption measurements performed for STO grown by pulsed laser deposition at room temperature (a-STO) with subsequent annealing at elevated temperatures to attain c-STO.

## II. RESULTS AND DISCUSSION

To obtain an adequate statistical representation of the structural properties of a-STO, ten separate MD liquid-quench realizations with the same conditions (density, composition, initial melting temperature, quench rate, equilibration temperature) were performed for each density, resulting in 70 independent MD quenches. Two additional MD realizations with density  $0.6$  and  $0.9\rho_c$  were obtained for completeness. At room temperature, each of the realizations was found to correspond to a stable solution with no energy drift and small thermal fluctuations in the total energy that represent a structure in equilibrium. The energy differences between the realizations with densities  $0.65\text{--}0.80\rho_c$  are within only  $0.02 \text{ eV/atom}$ , implying that a-STO samples with a density within this range may be obtained using the same deposition procedure and parameters.

An ensemble of the individual stable realizations at a given density represents a realistic sample of amorphous STO structure and, despite the energy distribution within each density set, the calculated energy-density relationship in a-STO follows a well-defined parabolic dependence, Fig. 1(a), left panel. A minimum with respect to the total energy averaged over ten realizations is observed at density  $\rho_a/\rho_c = 0.75$  for both the equilibrated at 300 K and the fully relaxed at zero K models. In addition, the models obtained after 300 K equilibration are relaxed to attain zero pressure structures [42]. The results reveal that the higher-energy configurations at either extremes of the initial density values fall close to the optimal density value of  $0.75\rho_c$ , Fig. 1(a), right panel. Thus the parabolic energy-density dependence obtained using a sufficient number of realizations and zero-pressure calculations predict the same optimal density of  $0.75\rho_c = 3.84 \text{ g/cm}^3$  for a-STO. The resulting amorphous structures with density  $0.75\rho_c$  and  $1.00\rho_c$ , along with a hypothetical structure of c-STO at  $0.75\rho_c$  density, modeled to illustrate that perovskite structure is completely destroyed at low density, are given in Fig. 1(b).

The room-temperature models were first characterized by evaluating the total and partial pair distribution functions (PDF) [43] with each plot representing an average over 5,000 MD configurations at 300 K, Fig. 2(a). The first two peaks of the total PDF are due to Ti-O bonds at  $\sim 1.90 \text{ \AA}$  and Sr-O bonds at  $\sim 2.50 \text{ \AA}$ . The changes in total PDF as a function of density are gradual [44]. The longer-range features are destroyed in all amorphous structures as well as in the hypothetical structure with  $0.75$  density, Fig. 2(a).

The vibrational density of states (VDOS) calculations provide crucial information about local bonding and an accurate assessment of the dynamical stability of a structural model. We find that the calculated normal modes for all amorphous models are real, confirming the dynamical stability of a-STO. The VDOS for a-STO and c-STO at  $0.75\rho_c$  are featureless, Fig. 2(b), confirming the loss of perovskite geometry as density decreases. The partial VDOS reveal broader contributions as compared to that for c-STO at crystalline density.

Next, the Fourier transform of the Sr and Ti K-edge EXAFS calculated for the MD-simulated a-STO models at several densities is compared to the available experimental EXAFS data in Fig. 3. The computational details, including the approach to calculate the spectra based on the amorphous models at 300 K is given in Appendix. The comparison reveals that the best agreement with experimental EXAFS [20] that claims tetrahedral environment of Ti, is obtained for the a-STO models with  $0.85\rho_c$ , Fig. 3, left panel. At other densities, the first peak for either Sr or Ti K-edge shifts away from the experimental EXAFS peak [44]. This is in accord with the opposite trends in Ti-O and Sr-O distances with decreasing density, discussed below. Repeating the same procedure for the experimental EXAFS [17] claiming octahedral environment of Ti, the best agreement for both Sr and Ti K-edge spectra is found for a-STO models at  $1.00\rho_c$ , Fig. 3, right panel. Thus the results suggest that the discrepancy in the two EXAFS measurements stems from different density in the experimental a-STO samples.

After the theoretical a-STO models were validated via excellent agreement with both EXAFS measurements, the

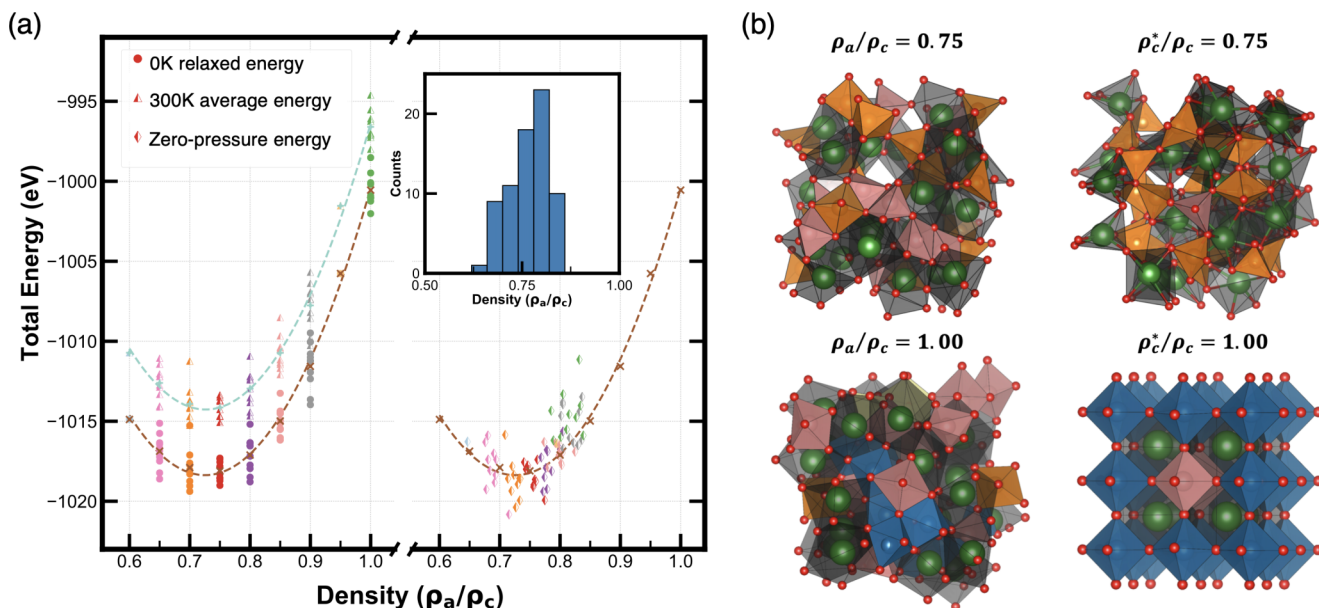


FIG. 1. (a) The average total energy for 72 melt-quench a-STO models after equilibration at 300 K for 5000 MD steps ( $\Delta$ ) and the total energy after the fixed-volume atomic relaxation at 0 K ( $\circ$ ). A second-order polynomial fit uses the average energies of 10 models at respective density ( $+$  and  $\times$ ) to reveal parabolic energy-density relationship for a-STO with an optimal value at  $0.75\rho_c$ . On the right, the total energy as a function of the density upon zero-pressure optimization ( $\diamond$ ). The polynomial fit of 0 K relaxation at fixed volume is shown here for comparison. The inset gives the distribution of zero-pressure densities. (b) 3D representation of simulation cells for a-STO at density  $0.75\rho_c$  and  $1.00\rho_c$  (left), and c-STO at density  $0.75\rho_c$  and  $1.00\rho_c$  (right). The Ti polyhedra are highlighted according to the effective coordination, [3,4]: orange, [4,5]: pink, [5,6]: blue, and [6,7]: yellow. All Sr atoms are shown in green with a gray polyhedron. The plots are made using VESTA software [38].

structures are studied in more detail. The O-Ti-O angle distribution provides key evidence that the symmetry of the Ti-O polyhedra changes in a-STO as compared to c-STO. The peak at  $90^\circ$ , that is characteristic of octahedral Ti in a perovskite structure, becomes much broader and gradually shifts toward  $100^\circ$ , whereas the peak at  $180^\circ$  is fully suppressed at lower

densities, Fig. 4(a), left panel. For an accurate description of the local (nearest-neighbor) environment in a-STO, the effective coordination number (ECN) and effective average distance ( $l_{\text{eff}}$ ) are calculated (see Appendix) for all Ti and Sr atoms in each a-STO model, Fig. 4(b). Compared to fixed cutoff calculations, the weighted averaging in individual M-O

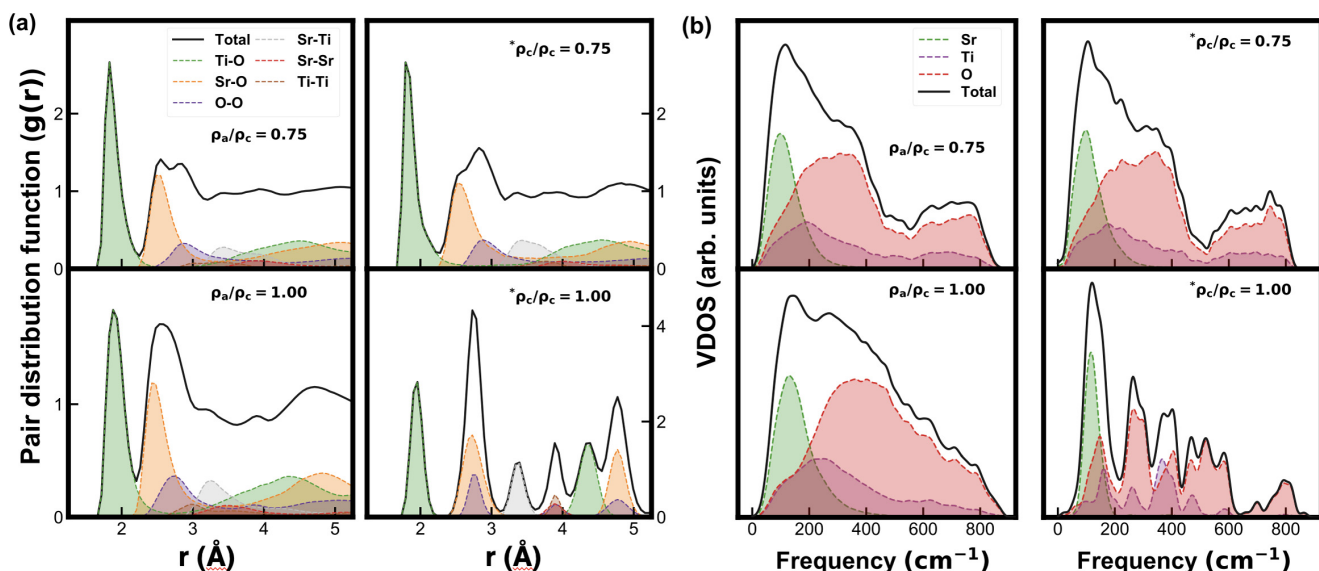


FIG. 2. (a) Total and partial pair distribution function  $g(r)$  for STO at density  $0.75\rho_c$  and  $1.00\rho_c$  for two amorphous models (left) and two crystalline models (right) at 300 K. (b) The calculated vibrational density of states (VDOS) for a-STO and c-STO at densities  $0.75\rho_c$  and  $1.00\rho_c$ . The VDOS is decomposed to elemental contributions with  $g_{\text{total}}(\omega) = \sum_{\alpha} g_{\alpha}(\omega)$ .

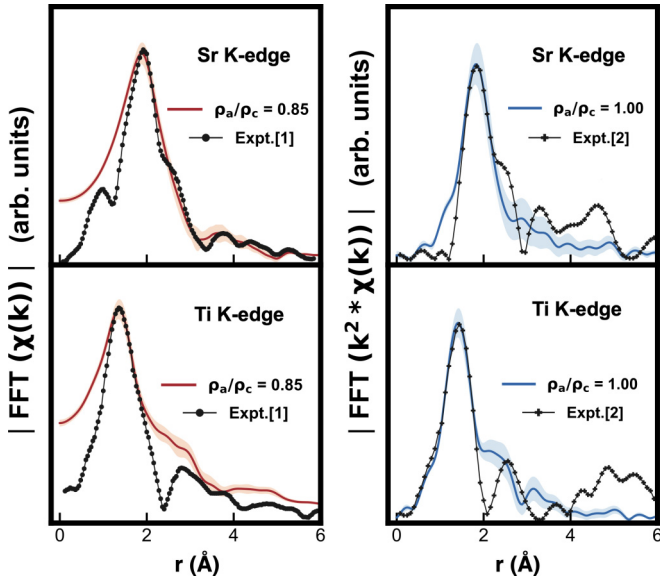


FIG. 3. The calculated Sr K-edge and Ti K-edge EXAFS spectra for a-STO at density  $0.85\rho_c$  compared with experimental EXAFS [20] claiming tetrahedral Ti (left) and a-STO at density  $1.00\rho_c$  compared with experimental EXAFS [17] claiming octahedral Ti (right). The lines represent the average spectra over ten realizations at the respective density, and the shading represents deviation among the realizations.

polyhedra represents a better approach to characterize the local environment because it accounts for strong polyhedra distortions represented by the tails in distance and angle distributions.

Figure 4(a), right panel, shows that the shorter Ti-O bond length originates primarily from a larger fraction of the Ti atoms with low effective coordination,  $ECN = [3, 4]$  and, to a lesser extent, from those with  $ECN = [4, 5]$ . The Ti-O distance for the highly coordinated Ti,  $ECN = [5, 6]$ , increases as the density decreases to  $0.85\text{--}0.75\rho_c$ . At  $0.65\rho_c$ , the fraction of octahedrally coordinated Ti atoms diminishes, pointing out that a complete coordination transformation has occurred. However, even at density  $1.0\rho_c$  for a-STO, rather than being confined to a distorted octahedral environment [17], the Ti atoms assume a wide range of coordination values, [4, 5.6], as revealed from the plot of  $ECN$  as a function of  $l_{\text{eff}}$  for individual Ti-O polyhedra, Fig. 4(b), and from the effective coordination distributions [44]. Reduction in density leads to a gradual shift of the broad  $ECN(\text{Ti})$  distribution toward lower values. The changes are comparable to those obtained for a well-studied a-TiO<sub>2</sub> where a wide range of Ti coordination values was reported [44].

Upon amorphization, Sr coordination is reduced by as much as 49%, which is a greater change than that for Ti (28%). This should be expected for the ionic and covalent bonding, respectively. Our theoretical  $ECN(\text{Sr})$  value at  $0.85\rho_c$  is in a good agreement with the experimental value of  $6.5 \pm 0.4$  [20]. We find that both  $ECN$  and  $l_{\text{eff}}$  for Ti-O increase with an increase in density [44], remaining well below the crystalline  $ECN(\text{Ti})$  of 5.5. An opposite trend is found for Sr-O bond-length: it decreases with an increase in density, while the  $ECN$  for Sr-O increases from 4.72 to 6.56, both

being much lower than the  $ECN(\text{Sr})$  of 10.40 in crystalline STO.

The opposite trends observed for the Ti-O and Sr-O distances as density decreases imply significant changes in the polyhedra network in the disordered oxide. Importantly, while the Ti-Sr face-sharing that is a signature of perovskite structure, is completely destroyed in the hypothetical low-density c-STO and all a-STO models, the number of corner-shared Ti-Ti pairs is nearly unchanged upon amorphization, Fig. 4(b), inset. The preserved corner-shared Ti-Ti network [44] may explain the observed polarization in a-STO [17].

In c- and a-STO, the valence band is formed from the O  $2p$  states and the conduction band is formed from the Ti  $3d$  states, Fig. 5(a). Ti- $d$ -O- $p$  orbital overlap governs the energy splitting between the bonding and antibonding states and, therefore, it controls the band gap of STO. Shorter Ti-O bond length implies larger orbital overlap; accordingly, our HSE calculated direct band gap at  $\Gamma$  point increases from 3.48 eV in c-STO to 3.55 eV at  $1.0\rho_c$  and to 4.20 eV at  $0.75\rho_c$  in a-STO, Fig. 5(a), in agreement with our optical absorbance measurements, Fig. 6(a). The calculated band gap for c-STO is in a good agreement with previous studies [45,46]. The band gap increase in a-STO is primarily associated with lower density as evident from the comparison of the band-gap values at densities  $1.0\rho_c$  and  $0.75\rho_c$  for both c-STO and a-STO (the calculated band gap for hypothetical c-STO at  $0.75\rho_c$  is 4.09). Specifically, the decrease in density increases the band gap by nearly 20% in both amorphous and crystalline (hypothetical) STO. When the density is fixed to either value, disorder increases the band gap only slightly, by 2%–3%. An increase in bandgap value upon amorphization is also observed in a-TiO<sub>2</sub> [26–28].

Furthermore, the strong dependence of the Ti- $d$  density of states on the Ti coordination, Fig. 5(b), helps explain the observed broadening and shift of the Ti  $e_g$  peak toward the  $t_{2g}$  peak in the XAS Ti L-edge spectra, Fig. 6(b). Charge density distribution calculated within consecutive energy windows in the conduction band, Fig. 6(c), reveals that the bottom of the band is governed by the  $t_{2g}$  states of edge-shared Ti-Ti pairs that do not exist in perovskite structure and appear due to disorder in a-STO. Importantly,  $t_{2g}$  orbitals are found for six-, five-, and fourfold Ti atoms within 1 eV above the Fermi level ( $E_F$ ) in a-STO, Fig. 6(c), top panel. The  $e_g$  orbitals contributions arise at 2 eV above  $E_F$  in c-STO, whereas a region with intermixed  $t_{2g}$  and  $e_g$  orbitals is found in a-STO within 1–2 eV above  $E_F$ , in accordance with the observed broadening of the XAS peaks. At higher energies, at 2–3 eV above  $E_F$ , the  $e_g$  character is mainly associated with highly symmetric four-coordinated Ti found in a-STO, Fig. 6(c), bottom right panel.

### III. CONCLUSIONS

In summary, our comprehensive first-principles investigations aimed at establishing the role of disorder on the short-range structural characteristics of STO, reveal a shallow parabolic energy-density dependence in a-STO with an optimal density at 0.75 of the crystalline STO density. The strong density dependence of the Ti effective coordination that changes from 4.67 at the crystalline density of  $5.12 \text{ g/cm}^3$  to

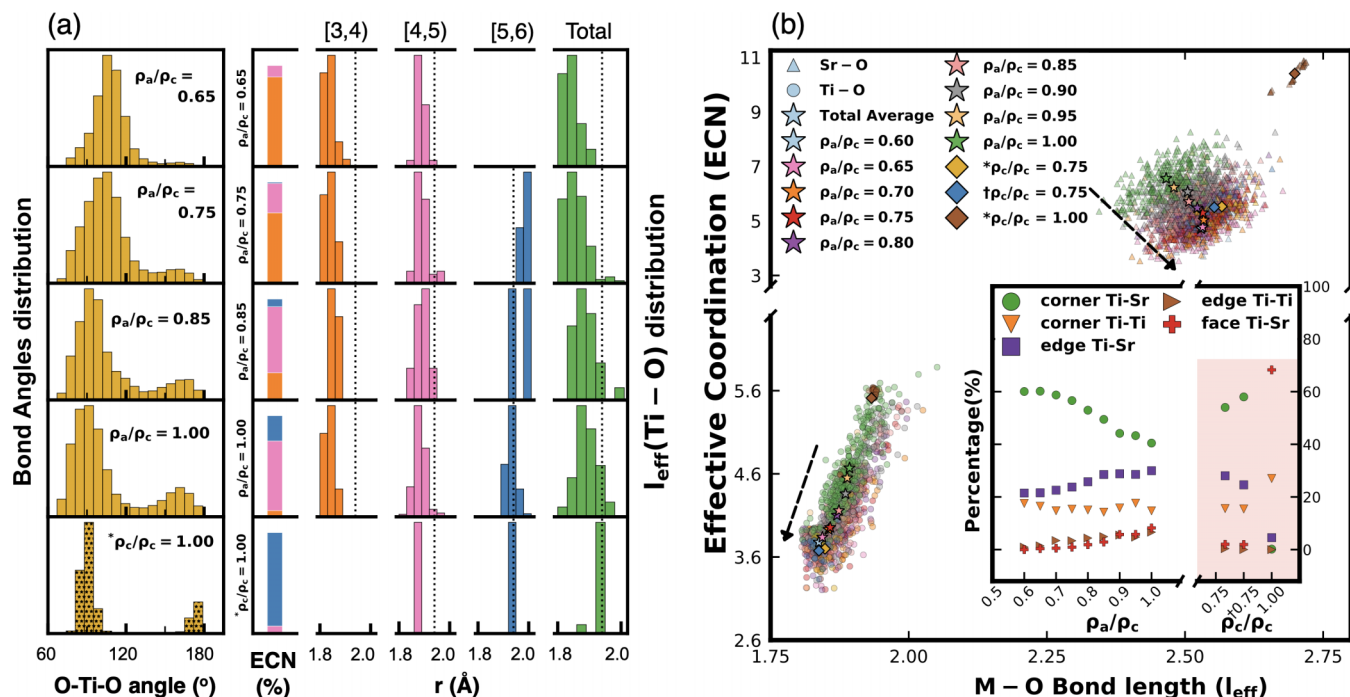


FIG. 4. Structural signatures of a-STO at 300 K across density range. (a) Left: O-Ti-O angle distribution for selected a-STO and c-STO at selected densities. (a) Right: Ti-O bond length distribution of differently coordinated Ti at different density. (b) Effective coordination number (ECN) as a function of effective bond length ( $l_{\text{eff}}$ ) of individual Ti ( $\circ$ ) and Sr ( $\Delta$ ) atoms in a-STO and c-STO. The average values over ten realizations at each density for amorphous ( $\star$ ) and crystalline ( $\diamond$ ) models ( $\dagger 0.75$  is for stoichiometric c-STO). Black arrows show the direction of decreasing density, highlighting opposite trends for Sr-O and Ti-O bond lengths. The inset shows percentage of sharing environment for Ti atoms.

3.96 at  $3.84 \text{ g/cm}^3$ , help explain two seemingly contradictory experimental EXAFS observations. Moreover, the calculated electronic properties of a-STO are in excellent agreement with the observed increase of the band gap and broadening of the Ti- $d$  XAS peaks in a-STO. The results reveal that the reduced

coordination of Ti and Sr does not destroy the corner-shared Ti-O network and does not lead to in-gap states in the disordered phase—in accord with the observed unique properties of amorphous STO, including polarity and excellent resistivity switching. The microscopic insights into disorder-induced

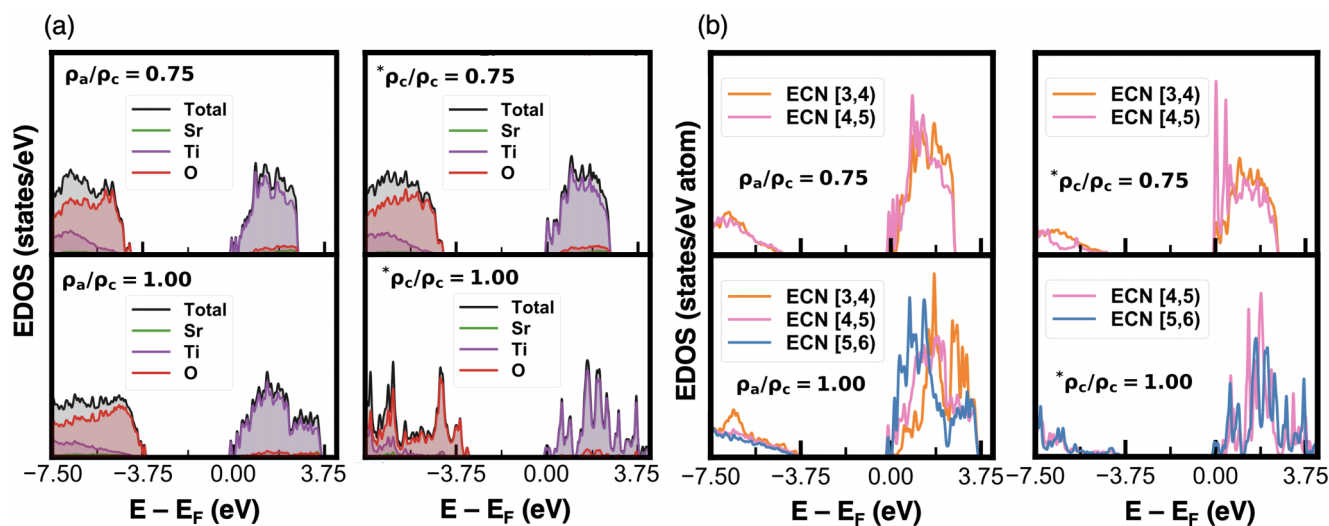


FIG. 5. Electronic and optical properties of STO calculated using hybrid density functional approach for the structures relaxed at 0 K. (a) Left: total and partial electronic density of states (EDOS) of a-STO with density  $0.75\rho_c$  and  $\rho_c$ . No in-gap states appear in the substoichiometric a-STO despite the large fraction of low-coordinate Ti atoms, cf. Fig. 4(b). (a) Right: EDOS of c-STO at densities  $0.75\rho_c$  (hypothetical structure) and  $\rho_c$ . (b) The EDOS (eV/states/atom) for specific Ti atoms with ECN [3,4], [4,5], and [5,6] are given for the crystalline and amorphous STO structures with the density as shown.

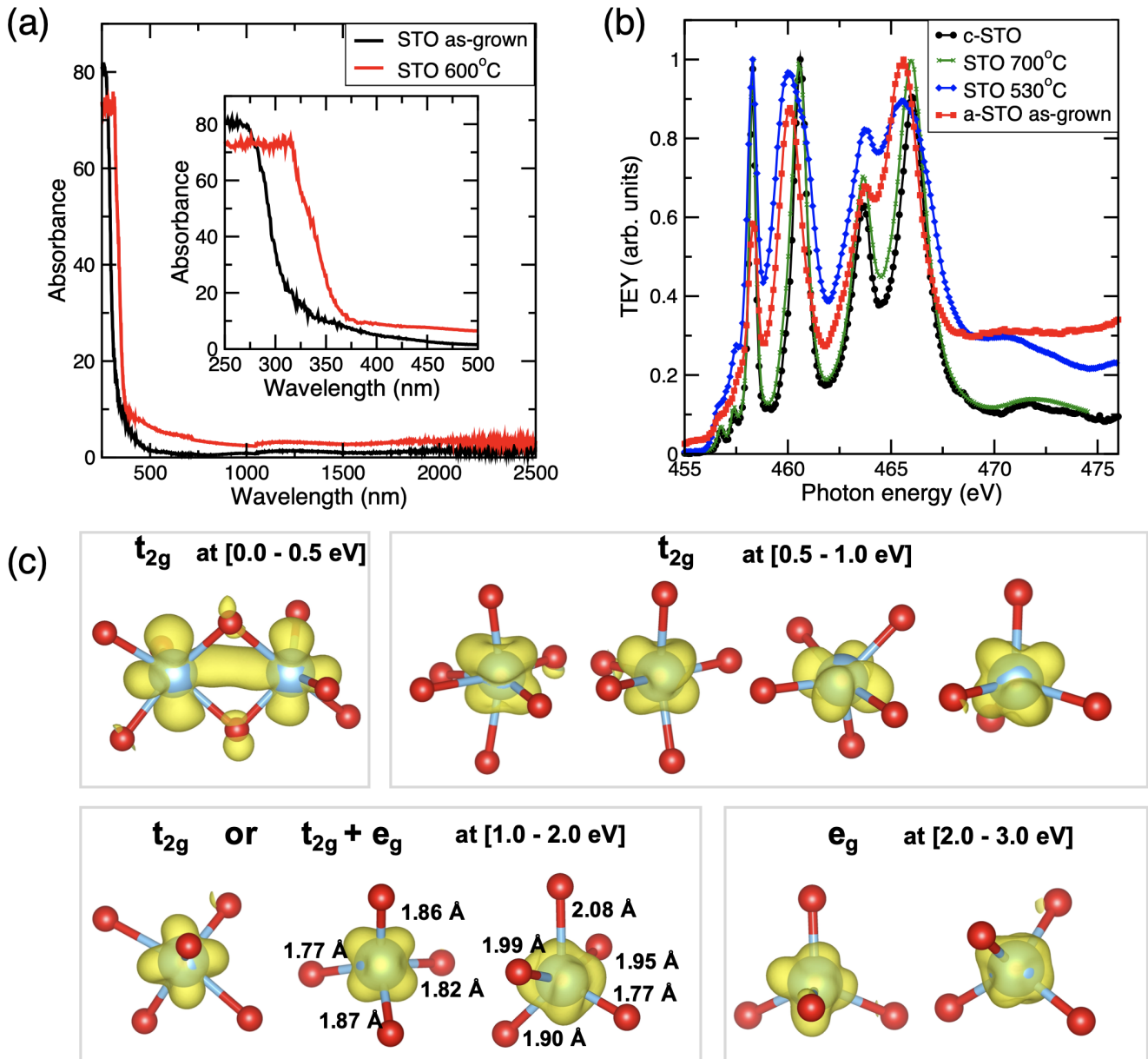


FIG. 6. (a) Optical absorbance measured for as-grown (room temperature) a-STO and for STO sample annealed at 600 °C. (b) X-ray absorption spectroscopy for Ti L-edge spectra for as-grown and annealed STO samples. (c) Charge density distribution calculated at specified energy ranges above the Fermi level ( $E_F = 0$  eV) and shown for select representative Ti atoms in a-STO with density  $0.75\rho_c$ . The calculated Ti-O distances for the strongly distorted polyhedra with intermixed  $t_{2g}$  and  $e_g$  orbitals are shown. The structures and charge densities are plotted with VESTA [38].

changes described in this work are instructive for further investigations of complex properties of a-STO and related amorphous “perovskite” materials.

#### ACKNOWLEDGMENTS

We are grateful to Alex Zunger for initiating the collaboration and for helpful discussions. The authors acknowledge the support from the National Science Foundation (NSF)-DMREF program (Grants DMR-1729779, DMR-1842467) and NSF Major Research Instrumentation Grant No. OAC-1919789 for computational resources.

#### APPENDIX: THEORETICAL METHODS

##### 1. Computational simulations and calculations

The amorphous models of STO are generated using first-principles molecular dynamics (MD) “melt-quench” approach [39] as implemented in Vienna *ab initio* simulation package (VASP) [40,41] with PBE functionals [47]. We have chosen a crystalline STO supercell with 26 Sr, 26 Ti, and 77 O as our initial structure; all a-STO models are substoichiometric to avoid formation of  $O_2$  defect during the quench process [37,48]. This initial structure was melted above the melting temperature of STO at 3600 K for 10 ps, and then subsequently quenched to 2500 K at a cooling rate of 100 K/ps.

The structure at 2500 K was cooled to 100 K at a cooling rate of 200 K/ps (the slower rate of 5 K/ps was also investigated [44]); the final structure at 100 K was again heated and equilibrated at 300 K for 10 ps in order to ensure the stable energy solution and to capture the structure in the presence of room temperature fluctuations. In addition, a slower quench rate of 5 K/ps was employed for a-STO with crystalline density to determine the role of quench rate on the Ti coordination. The results are included in Ref. [44].

We have prepared ten realizations for each density at  $\rho_a/\rho_c = 0.65, 0.70, 0.75, 0.80, 0.85, 0.90,$  and 1.0 as well as one realization for densities  $\rho_a/\rho_c = 0.60$  and 0.95 with coordinates of the structure at 3600 K (without velocities) used to create multiple realizations. The Nose-Hoover thermostat [49,50] was used to control temperature oscillations, with NVT ensemble and time step of 2 fs. In order to facilitate computational efficiency, a low cutoff of 260 eV is chosen for melt and quench step; a larger cutoff of 400 eV is used for final equilibration at 300 K, and  $k$ -point sampling is restricted to  $\Gamma$  point only in all MD simulations. The electronic convergence was determined by the energy difference of  $10^{-4}$ . A total of 31.5 ps simulation time was used which is a typical timescale used to prepare amorphous models. We have modeled ten independent MD realizations for each density; this number appears to be sufficient to obtain parabolic nature of the energy-density curve.

## 2. Zero pressure calculations

For the purpose of estimating an optimal density, a further minimization of forces and energies of the 72 a-STO models were performed. This relaxation is different from the finite volume relaxation, because it consist of unconstrained volume change and cell shape (lattice vectors allowed to change) to attain zero pressure. This was carried out using “ISIF =3” option with VASP package. We have implemented a higher energy cutoff of 600 eV with energy difference of  $10^{-8}$  for the electronic convergence and Hellmann-Feynman force criteria below 0.005 eV/Å on each atom for the ionic convergence. The zero pressure minimization was carried out with a single  $k$  point ( $\Gamma$  point).

## 3. Effective coordination calculations

The effective coordination and effective bond length were computed for individual Ti and Sr atoms in each of the 72 a-STO models using the definitions given in work of Hoppe *et al.* [51,52]:

$$l_{\text{eff}} = \frac{\sum_i l_i \exp\left[1 - \left(\frac{l_i}{l_{\text{min}}}\right)^6\right]}{\sum_i \exp\left[1 - \left(\frac{l_i}{l_{\text{min}}}\right)^6\right]}, \quad (\text{A1})$$

$$\text{ECN} = \sum_i \exp\left[1 - \left(\frac{l_i}{l_{\text{eff}}}\right)^6\right]. \quad (\text{A2})$$

The effective coordination number (ECN) differs from classical coordination number defined as the number of anions surrounding a cation within a fixed cutoff distance which is usually determined from the tail in the distance distribution function and is the same for all cations in the structure. In

contract, ECN [Eq. (A2)] is calculated as a sum of weighted contributions from each bond with respect to the effective average distance in the given polyhedron [51,52]. As a result, it eliminates the contributions from long-distance bonds that correspond to noninteracting metal-oxygen pairs. The effective coordination number is a noninteger number and is typically lower than a fixed cutoff coordination and accounts for the strong Ti-O and Sr-O polyhedra distortions represented by the wide angle distributions and variance in bond lengths for each individual metal atom.

## 4. Hybrid calculations

Accurate prediction of the electronic properties requires hybrid calculations, because PBE typically underestimates the band gap. We have implemented hybrid Heyd-Scuseria-Ernzerhof (HSE06) approach [53,54], with a mixing parameter of 0.25 and a screening parameter  $\alpha$  of 0.30 Å consistent with previous HSE06 calculation of c-STO [45,46]. The HSE06 calculations were performed for fully relaxed structures within converged PBE calculations. An energy cutoff of 500 eV, electronic convergence criteria of  $10^{-6}$  and eight-irreducible  $k$  points were used for the HSE calculations.

## 5. Dynamical calculations

In order the compute phonons at  $\Gamma$  point, ee rereaxed out models with energy cutoff of 600 eV, electronic convergence criteria of  $10^{-8}$  and minimum force of 0.005 eV/Å on each atom for ionic convergence. The phonons were calculated using finite-difference methods. The dynamical matrix was computed by calculating forces on each atom followed by a displacement of 0.015 Å in six directions ( $\pm x, \pm y, \pm z$ ). The vibrational density of states (VDOS) were evaluated using Gaussian broadening of 12  $\text{cm}^{-1}$ .

## 6. EXAFS calculations

To compare the structural properties of a-STO with experiment, we computed extended x-ray absorption fine structure (EXAFS) spectra using *ab initio* code FEFF8-LITE [55,56] and Fourier transformation was performed using the IFEFFIT software [57]. The results are given in Fig. 3. The EXAFS spectra was evaluated by taking cluster radius of 5.5 Å centered at the absorbing atom (Sr or Ti). The obtained K-edge spectra from each cluster was averaged to get an average spectra. The averaged spectra was used to carry out Fourier transformation via IFEFFIT software [57]. We have used Hanning window function with Fourier transformation range of 2.6-11.6 [FFT( $\chi(k)$ )] and 2.0-8.5 [FFT( $k^2 * \chi(k)$ )] for Sr atoms consistent with the experimental EXAFS [17,20]. Similarly, Fourier transformation range of 3.45-10.3 [FFT( $\chi(k)$ )] and 2.5-9.0 [FFT( $k^2 * \chi(k)$ )] was used for Ti atoms in consistent with the experimental EXAFS.

In order to capture room temperature fluctuations and to smooth EXAFS spectra, we have considered 41 snapshots from the 5000 ionic step MD at 300 K for single realization. These 41 snapshots were chosen beginning from the 1000th ionic step at an interval of 100 ionic steps. Similarly, those densities which have ten realizations we have chosen 11 snapshots beginning from the 1000th ionic step at an interval of

400 ionic steps. Thus the EXAFS spectra shown in this work is an average over 41 snapshots (for density with one realization only) and an average over 110 snapshots (for densities with ten realizations).

### 7. Hypothetical crystalline STO calculations

A hypothetical crystalline STO with reduced density was obtained by increasing the volume of the supercell (i.e., the lattice parameter of the cubic supercell), while keeping the same number of atoms in the supercell. The positions of all atoms in the supercell with the increased volume were relaxed via the total energy and atomic force minimization to allow for the metal-oxygen distances to attain optimal values. The short-range structural parameters (the pair distribution function, the average Sr and Ti coordination and distances as well

as vibrational density of states) of the hypothetical crystalline STO and amorphous STO with 75% density were compared, revealing a similar behavior.

### 8. Experimental STO growth and characterization

Amorphous STO thin films were grown by pulsed laser deposition at room temperature on SrTiO<sub>3</sub> (001) single crystal substrate (TiO<sub>2</sub> termination). Subsequent annealing at 280 °C, 446 °C, 525 °C, 562 °C, 600 °C, 670 °C, and 727 °C was employed. X-ray absorption spectroscopy (XAS) for Ti L-edge spectra are performed for select STO films to study the evolution of the XAS spectra as a function of different thermal treatments. Optical absorbance measurements were performed for the room-temperature (as-grown) and annealed at 600 °C STO films.

- 
- [1] A. Brinkman, M. Huijben, M. van Zalk, J. Huijben, U. Zeitler, J. C. Maan, W. G. van der Wiel, G. Rijnders, D. H. A. Blank, and H. Hilgenkamp, *Nat. Mater.* **6**, 493 (2007).
- [2] A. Erba, K. E. El-Kelany, M. Ferrero, I. Baraille, and M. Rérat, *Phys. Rev. B* **88**, 035102 (2013).
- [3] G. Shirane and Y. Yamada, *Phys. Rev.* **177**, 858 (1969).
- [4] J. F. Schooley, W. R. Hosler, and M. L. Cohen, *Phys. Rev. Lett.* **12**, 474 (1964).
- [5] A. B. Posadas, K. J. Kormondy, W. Guo, P. Ponath, J. Geler-Kremer, T. Hadamek, and A. A. Demkov, *J. Appl. Phys.* **121**, 105302 (2017).
- [6] C. Lin and A. A. Demkov, *Phys. Rev. Lett.* **111**, 217601 (2013).
- [7] L. Yu and A. Zunger, *Nat. Commun.* **5**, 5118 (2014).
- [8] K. Morii, H. Kawano, I. Fujii, T. Matsui, and Y. Nakayama, *J. Appl. Phys.* **78**, 1914 (1995).
- [9] K.-S. Liu, Y.-J. Chen, G. Jamn, and I.-N. Lin, *Appl. Phys. Lett.* **75**, 2647 (1999).
- [10] Y. Chen, N. Pryds, J. E. Kleibecker, G. Koster, J. Sun, E. Stamate, B. Shen, G. Rijnders, and S. Linderoth, *Nano Lett.* **11**, 3774 (2011).
- [11] D. J. McClure and J. R. Crowe, *J. Vac. Sci. Technol.* **16**, 311 (1979).
- [12] F. Pontes, E. Longo, E. Leite, E. Lee, J. Varela, P. Pizani, C. Campos, F. Lanciotti, V. Mastellaro, and C. Pinheiro, *Mater. Chem. Phys.* **77**, 598 (2003).
- [13] H. Nili, S. Walia, S. Balendhran, D. B. Strukov, M. Bhaskaran, and S. Sriram, *Adv. Funct. Mater.* **24**, 6741 (2014).
- [14] T. Ahmed, S. Walia, J. Kim, H. Nili, R. Ramanathan, E. L. H. Mayes, D. W. M. Lau, O. Kavehei, V. Bansal, M. Bhaskaran, and S. Sriram, *Nanoscale* **9**, 14690 (2017).
- [15] S. Yadav and S. Ghosh, *ACS Appl. Mater. Interfaces* **8**, 10436 (2016).
- [16] K. Morii, T. Matsui, H. Tsuda, and H. Mabuchi, *Appl. Phys. Lett.* **77**, 2361 (2000).
- [17] A. I. Frenkel, D. Ehre, V. Lyahovitskaya, L. Kanner, E. Wachtel, and I. Lubomirsky, *Phys. Rev. Lett.* **99**, 215502 (2007).
- [18] D. Ehre, H. Cohen, V. Lyahovitskaya, and I. Lubomirsky, *Phys. Rev. B* **77**, 184106 (2008).
- [19] E. Wachtel and I. Lubomirsky, *Adv. Mater.* **22**, 2485 (2010).
- [20] S. Blonkowski, E. Defay, and X. Biquard, *Phys. Rev. B* **79**, 104108 (2009).
- [21] J. Balachandran, L. Lin, J. S. Anchell, C. A. Bridges, and P. Ganesh, *J. Phys. Chem. C* **121**, 26637 (2017).
- [22] N. A. of Sciences, Engineering, and Medicine, *Frontiers of Materials Research: A Decadal Survey* (The National Academies Press, Washington, DC, 2019).
- [23] Y. Chen, M. H. Yusuf, Y. Guan, R. B. Jacobson, M. G. Lagally, S. E. Babcock, T. F. Kuech, and P. G. Evans, *ACS Appl. Mater. Interfaces* **9**, 41034 (2017).
- [24] S. A. Rigter, X. L. Quinn, R. E. Kumar, D. P. Fenning, P. Massonnet, S. R. Ellis, R. M. A. Heeren, K. L. Svane, A. Walsh, and E. C. Garnett, *Adv. Funct. Mater.* **31**, 2010330 (2021).
- [25] M. Matsui and M. Akaogi, *Mol. Simul.* **6**, 239 (1991).
- [26] H. Tang, H. Berger, P. Schmid, F. Lévy, and G. Burri, *Solid State Commun.* **87**, 847 (1993).
- [27] A. Amtout and R. Leonelli, *Phys. Rev. B* **51**, 6842 (1995).
- [28] B. Prasai, B. Cai, M. K. Underwood, J. P. Lewis, and D. A. Drabold, *J. Mater. Sci.* **47**, 7515 (2012).
- [29] A. Pedone, G. Malavasi, M. C. Menziani, A. N. Cormack, and U. Segre, *J. Phys. Chem. B* **110**, 11780 (2006).
- [30] B. Guillot and N. Sator, *Geochim. Cosmochim. Acta* **71**, 4538 (2007).
- [31] E. Maras, N. Salles, R. Tétot, T. Ala-Nissila, and H. Jónsson, *J. Phys. Chem. C* **119**, 10391 (2015).
- [32] M. Durandurdu, *J. Am. Ceram. Soc.* **100**, 3903 (2017).
- [33] K. Yang, A. Kachmar, B. Wang, N. M. A. Krishnan, M. Balonis, G. Sant, and M. Bauchy, *J. Chem. Phys.* **149**, 094501 (2018).
- [34] N. A. Deskins, J. Du, and P. Rao, *Phys. Chem. Chem. Phys.* **19**, 18671 (2017).
- [35] J. Mavračić, F. C. Mocanu, V. L. Deringer, G. Csányi, and S. R. Elliott, *J. Phys. Chem. Lett.* **9**, 2985 (2018).
- [36] J. E. Medvedeva, D. B. Buchholz, and R. P. H. Chang, *Adv. Electron. Mater.* **3**, 1700082 (2017).
- [37] J. E. Medvedeva, I. A. Zhuravlev, C. Burris, D. B. Buchholz, M. Grayson, and R. P. H. Chang, *J. Appl. Phys.* **127**, 175701 (2020).
- [38] K. Momma and F. Izumi, *J. Appl. Cryst.* **41**, 653 (2008).
- [39] D. A. Drabold, *Eur. Phys. J. B* **68**, 1 (2009).
- [40] G. Kresse and J. Furthmuller, *Phys. Rev. B* **54**, 11169 (1996).
- [41] G. Kresse and D. Joubert, *Phys. Rev. B* **59**, 1758 (1999).
- [42] The system is relaxed using ISIF = 3 tag and higher energy cutoff in VASP. This allows the lattice vectors to change,



- resulting in a nonorthogonal cell with an optimal final volume that corresponds to minimized total energy configuration.
- [43] S. Le Roux and P. Jund, *Comput. Mater. Sci.* **49**, 70 (2010).
- [44] See Supplemental Material at <http://link.aps.org/supplemental/10.1103/PhysRevMaterials.6.075605> for effective coordination distributions at different cooling rates; three-dimensional plots of Ti-O polyhedra at different density and cooling rates; pair-distribution function for a-STO at seven different density values; EXAFS peak fitting; and a list of the structural properties for crystalline and amorphous TiO<sub>2</sub> as reported in literature [28,32,35,58].
- [45] R. Wahl, D. Vogtenhuber, and G. Kresse, *Phys. Rev. B* **78**, 104116 (2008).
- [46] C. Mitra, C. Lin, J. Robertson, and A. A. Demkov, *Phys. Rev. B* **86**, 155105 (2012).
- [47] J. P. Perdew, K. Burke, and M. Ernzerhof, *Phys. Rev. Lett.* **77**, 3865 (1996).
- [48] A. Walsh, J. L. F. Da Silva, and S.-H. Wei, *Chem. Mater.* **21**, 5119 (2009).
- [49] S. Nosé, *J. Chem. Phys.* **81**, 511 (1984).
- [50] W. G. Hoover, *Phys. Rev. A* **31**, 1695 (1985).
- [51] R. Hoppe, *Angew. Chem., Int. Ed. Engl.* **9**, 25 (1970).
- [52] R. Hoppe, S. Voigt, H. Glaum, J. Kissel, H. P. Müller, and K. Bernet, *J. Less-Common Met.* **156**, 105 (1989).
- [53] J. Heyd, G. E. Scuseria, and M. Ernzerhof, *J. Chem. Phys.* **118**, 8207 (2003).
- [54] J. Heyd, J. E. Peralta, G. E. Scuseria, and R. L. Martin, *J. Chem. Phys.* **123**, 174101 (2005).
- [55] J. J. Rehr, J. J. Kas, M. P. Prange, A. P. Sorini, Y. Takimoto, and F. Vila, *C. R. Phys.* **10**, 548 (2009).
- [56] J. J. Rehr and R. C. Albers, *Rev. Mod. Phys.* **72**, 621 (2000).
- [57] M. Newville, *J. Synchrotron Radiat.* **8**, 322 (2001).
- [58] D. T. Cromer and K. Herrington, *J. Am. Chem. Soc.* **77**, 4708 (1955).